Integration of efficient LaSrCoO₄ perovskite and polyacrylonitrile membrane to enhance mass transfer for rapid contaminant degradation

Na Yang [a,1], Jingchao Yu [a,1], Longfei Zhang [b], Yongli Sun [a], Luhong Zhang [a], Bin Jiang [a,*]

[a] School of Chemical Engineering and Technology, Tianjin University, Tianjin 300072, People's Republic of China
[b] School of Chemistry and Chemical Engineering, Tianjin University of Technology, Tianjin 300384, People's Republic of China

ABSTRACT

A₂BO₄-type perovskite with Ruddlesden-Popper structure performed favorable catalytic activity in the activation of peroxymonosulfate (PMS) for the degradation of organic pollutants than ABO₃, but the higher forming temperature limits its further application. In this work, a series of A-site Sr doped La₂CoO₄₋δ perovskites were prepared and used for the degradation of tetracycline hydrochloride (TC). The introduction of Sr lowered the formation temperature of the perovskite and improved the catalytic capability. The LaSrCoO₄ perovskite with 50 % Sr doping possessed the best TC degradation efficiency (complete degradation in 14 min). Besides, to overcome the mass transfer limitation caused by catalyst powder agglomeration and the difficulty of recovery, perovskite powder catalysts were embedded in polyacrylonitrile (PAN) ultrafiltration membrane by phase conversion method. The resulting PAN/LSC catalytic separation membranes achieved efficient degradation of TC due to the partial increase in the concentration of contaminants inside the membrane pores. The membrane embedded with 5 wt% LaSrCoO₄ perovskite degraded 94 % TC in 3 min, which improved over 24 % compared to the perovskite powder. The catalytic degradation mechanism of TC and the toxicity of the intermediates were then analyzed. The effectiveness of catalytic membranes in practical applications was also evaluated. Overall, PAN/LSC membranes provide the potential for rapid purification of organic wastewater.

1. Introduction

Water scarcity is an inevitable problem for the development of human society. With the frequent usage of drugs and the development of aquaculture, antibiotics represented by tetracycline hydrochloride (TC) are gradually accumulating in surface water basins, which not only causes water pollution issues, but also has the pitfall of leading to the evolution of drug-resistant strains, posing a major threat to aquatic organisms and human health [1–3]. According to the antibiotic pollution map of the Chinese Academy of Sciences, >6100 tons of TC are released into the soil and groundwater environment each year [4]. Traditional methods such as biodegradation and physical adsorption are difficult to completely remove TC owing to its poor biodegradability [5–8]. Thus, an increasing number of researches aim to find green, effective and cost-efficient technologies to achieve rapid TC degradation in water bodies [9].

Sulfate radical-based advanced oxidation processes (SR-AOPs) have emerged as a potential technology for the degradation of difficult

pollutants in wastewater treatment due to their high efficiency [10]. SR-AOPs generate sulfate radicals ($SO_4^{\bullet-}$) through the breakage of peroxy bonds (-O-O-) in peroxymonosulfates (PMS), and the $SO_4^{\bullet-}$ with strong oxidizing ability can achieve the oxidation or partial mineralization of pollutants [11]. PMS can be generated by heat, ultrasound, ultraviolet light, electro-chemical methods, transition metal and carbon-based catalysts, and integrated processes between them [12]. In particular, the use of catalysts for PMS activation has the advantage of high activation efficiency and low cost and energy input. Since homogeneous catalysis causes secondary pollution to water bodies and the recovery of catalyst is difficult to achieve [13]. A variety of heterogeneous catalysts (transition metal oxides, nitrides, sulfides, carbon-based materials, etc.) have been used to activate PMS for the degradation of organic pollutants [14–16]. In recent years, ABO₃-type perovskites have gradually gained increasing attention in order to further pursue higher catalytic activity. [17]. Typical ABO₃-type perovskite oxides generally include rare earth or alkaline earth metal cations at the A-site, transition metal cations at the B-site, and O anions. Perovskite oxide catalysts offer various

benefits, such as good structural stability and electron transfer capability [18]. In comparison with ABO_3-type perovskite, Ruddlesden-Popper-type perovskite with layered structure possesses better surface exchange and volume diffusion coefficients of oxygen and thus exhibits higher stability and redox ability [19]. This structure consists of n-layers of ABO_3 perovskite plates stacked along the c-axis with rock salt layers (AO), and the general formula of perovskite can be expressed as A_2BO_4 when n is 1 [20]. A_2BO_4-type perovskite has a good thermal stability and a high ionic conductivity. A few studies have applied A_2BO_4-type perovskite for the activation of PMS and demonstrated that $La_2CuO_{4-\delta}$, $La_2CoO_{4+\delta}$ and $LaSrCo_{0.8}Fe_{0.2}O_{4-\delta}$ catalysts have superior catalytic ability than ABO_3-type perovskite [21–23]. Noteworthy, the great design flexibility of perovskite oxide permits the adjustment of catalyst lattice structure together with the oxidation state of transition metal elements by simple doping strategy [24]. Recent studies have concluded that doping at the A-site of perovskite is an effective method to improve catalytic performance in heterogeneous catalysis [25]. Cheng et al. introduced Sr into the A-site of $LaFeO_3$ perovskite and found that the doped perovskite enhanced the degradation rate of 2,4-dichlorophenoxyacetic acid by 5.7 times [12]. Gao et al. similarly demonstrated that Sr doping at the A-site increased the surface oxygen vacancies of perovskite and substantially enhanced the activation efficiency of PMS [26]. However, the modification of A-site doping on the catalytic activity of A_2BO_4-type perovskite remains to be further investigated. Besides, the synthesis of Co-based A_2BO_4 perovskite with the high catalytic activity is often accompanied by high pressure or temperature above 1000 °C, which limits further applications.

The application of perovskite catalysts in SR-AOPs still faces some significant challenges. The leaching of toxic metal ions and the difficulty of recovering the powder catalyst are inevitable problems for the long-term operation of perovskite catalysts [27]. Besides, natural organic matter (NOM) in the wastewater may potentially cover the active site of the catalyst and negatively affect the degradation [28]. To address these issues, loading heterogeneous catalysts into membrane substrates with selective separation capabilities is a promising concept [29–31]. Under external pressure, the effluent flows through the catalytic membrane, and large-molecule pollutants are blocked by size sieving, while small-molecule organic pollutants enter the membrane pores and combine with the uniformly dispersed catalysts, thus achieving the simultaneous separation/degradation process [32,33]. This continuous operation not only contributes to the rapid removal of degradation products from the catalyst surface and improves the degradation efficiency, but also helps to reduce the leaching of metal ions from the catalyst [34]. In addition, the tortuous path of the membrane pores leads to an increased partial concentration of contaminants, which strengthens the mass transfer and therefore contributes to the degradation efficiency of the catalyst [35]. Nevertheless, the activity of catalytic membranes remains to be further improved, despite some studies have attempted to combine perovskite catalysts with membranes.

Herein, A-site Sr-doped $La_2CoO_{4-\delta}$ perovskite catalysts were synthesized by a typical sol-gel method at a lower calcination temperature and the effect of Sr introduction on the catalytic activity was investigated. Then, the LSCx perovskite crystals were embedded in PAN membranes by phase transformation method. The obtained PAN/LSC catalytic separation membranes exhibited good permeation performance and excellent TC degradation under various operating conditions. In addition, the anti-pollution properties of the membranes were tested in the presence of NOM, and the catalytic membranes exhibited efficient synergy of separation/degradation performance. Accordingly, the catalytic membrane displayed favorable resistance to the interference of inorganic anions and exhibited efficient catalytic performance in different water matrices. Subsequently, the stability of the catalytic membranes, the reaction mechanism and the toxicity of the intermediates were analyzed. Finally, by comparison with other catalytic membranes, the PAN/LSC membrane exhibited desirable separation and degradation performance.

2. Experimental section

2.1. Materials

Peroxymonosulfate ($2KHSO_5 \cdot KHSO_4 \cdot K_2SO_4$), Cobalt nitrate hexahydrate ($Co(NO_3)_2 \cdot 6H_2O$), Lanthanum nitrate hexahydrate ($La(NO_3)_3 \cdot 6H_2O$), Sodium bicarbonate ($NaHCO_3$) and tetracycline hydrochloride (TC) were purchased from Shanghai Macklin Biochemical Co., Ltd. (China). Citric acid, Sodium nitrate ($NaNO_3$), Potassium dihydrogen phosphate (KH_2PO_4) and strontium nitrate ($Sr(NO_3)_2$) were provided by Shanghai Aladdin Chemical Reagent Co., Ltd. (China). Methanol (MeOH), furfural (FFA), Sodium chloride (NaCl), ammonium hydroxide ($NH_3 \cdot H_2O$), and tert-butyl alcohol (TBA) were supplied by Tianjin Guangfu Chemical Reagent Co., Ltd. (China). *N*-methyl pyrrolidone (NMP), PAN powder (Mw = 150,000 $g \cdot mol^{-1}$) and Humic acid (HA) were obtained from Tianjin Kermel Chemical Reagent Co., LTD (China). All chemicals were used directly with no further purification.

2.2. Synthesis of perovskite catalysts

The Sr dropped $La_2CoO_{4-\delta}$ perovskites were prepared by citrate sol-gel method according to the method of Huan et al. [36]. As shown in Fig. S1, the appropriately weighed $La(NO_3)_3 \cdot 6H_2O$, $Co(NO_3)_2 \cdot 6H_2O$, Sr$(NO_3)_2$, and citric acid were mixed in the appropriate molar ratio and dissolved in deionized water. Wherein, the mole ratio of metal cations to citric acid was 1:1.25. The solution was then stirred in the water bath at 80 °C for several hours until most of the water was evaporated to form a gel. The resulting gel was dried at 120 °C for 3 h to remove water and then got pink fluffy precursors. The precursor was then ground to powder and calcined at 180 °C for 2 h to decompose the citric acid. The temperature was then increased to 850 °C at a rate of 5 °C/min and maintained for 6 h. The resulting powder catalysts were labeled as LSCx according to the molar ratio of Sr at the A site in the perovskite, for example, when Sr occupied 50 % of the A site in the perovskite, the obtained $LaSrCoO_4$ was named as LSC50. In addition, $LaCoO_3$ (LCO) and $La_{0.5}Sr_{0.5}CoO_3$ (LSCO) were prepared using the same process with the calcination temperature reduced to 550 °C and the calcination time reduced to 4 h.

2.3. Fabrication of PAN/LSC catalytic membrane

The PAN/LSC catalytic membrane was prepared by the phase transition method [37]. First, several amounts of LSC perovskite catalyst were added to 8.8 g NMP solution and kept under ultrasonication for 30 min to make the catalyst uniformly dispersed. Then, 1.2 g of PAN powder was added into the solution and stirred in the water bath at 70 °C for 8 h. The obtained homogeneous casting solution was placed in a vacuum atmosphere at 60 °C for 12 h to eliminate bubbles. Afterward, the casting solution is slowly poured onto a neat glass plate and scraped with a 200 μm casting knife. Then, the glass plates were immersed in a water bath and kept for 36 h to complete the phase transformation process. The prepared PAN/LSC catalytic membranes were labeled as PAN/LSC-y membranes, where y is 1, 2, 3, 4, 5, 6, as the LSC50 catalyst content of 1 to 6 wt%, respectively.

2.4. Characterization

The crystalline phase of the synthesized perovskite was analyzed using X-ray Diffraction (XRD, Bruker-D8, Germany). Scanning Electron Microscopy (SEM, Hitachi S4800, Japan) and Transmission Electron Microscopy (TEM, JEM-F200 Japan) were used to obtain the morphologies of the LSC catalyst and catalyst membranes, while the elemental spectra of the catalyst and the cross sections of the catalyst membrane were examined using energy dispersive spectroscopy. X-ray Photoelectron Spectrometer (XPS, Thermo Scientific K-Alpha, USA) was used to analyze the chemical composition of the catalyst prior to and following

the reaction. The hydrophilicity of PAN/LSC-x membranes were characterized via water contact angle, observed and calculated at 25 °C by the Contact Angle Measuring Instrument (Powereach, China). The concentration of tetracycline hydrochloride was determined by Ultraviolet-visible Spectrophotometer (UV–vis 4802S, Unico, USA). In addition, intermediates during TC mineralization were analyzed using a High Performance Liquid Chromatography-tandem Mass Spectrometry (Thermo Vanquish UHPLC-LTQ XL, USA). Electron Paramagnetic Resonance (EPR, Bruker EMXplus-6/1, Germany) with 2,2,6,6-tetra-methyl-4-piperidinol (TEMP) and 5,5-dimethyl-1-pyrroline n-oxide (DMPO) as spin trapping agents was used to detect reactive oxygen species during the course of the reaction. The content of each constituent element of the catalyst embedded in the membrane and the leaching of metal ions from different catalysts and membranes were examined with Inductively Coupled Plasma Optical Emission Spectrometry (ICP-OES, Thermo Fisher iCAP PRO, USA).

2.5. Degradation performance of perovskite catalyst

The degradation performance of perovskite catalysts was evaluated by the rate of contaminant removal by activated PMS. In a typical procedure, 10 mg of perovskite powder was added to 200 mL of 15 ppm TC aqueous solution with constant stirring at 25 °C in the water bath. After 10 min, the catalyst has reached adsorption/desorption equilibrium. Then 0.5 mmol of PMS was added to the solution. A few solutions were periodically extracted and filtered with a 0.22 μm PVDF membrane. The UV–vis spectroscope was applied to detect the TC content at 357 nm.

In this test, the degradation rate of TC could be approximated by first order reaction. Therefore, the reaction rate can be analyzed by kinetic equations (Eq. (1)).

$$ln\frac{C}{C_0} = -kt \tag{1}$$

where C (mg·L^{-1}) is the TC concentration at instant t, while C_0 (mg·L^{-1}) refers to the concentration of initial TC, k (min^{-1}) means the kinetic rate constant, and t (min) represents the reaction time.

2.6. Assessment of the separation and degradation capacity of membranes

The separation and degradation performance of the membranes was evaluated using a cross-flow device with an effective filtration area of 7 cm^2. Before use, the membranes were pressurized to 0.15 MPa for 0.5 h, after which the pressure was lowered to 0.1 MPa and the pure water flux was calculated using Eq. (2).

$$J = \frac{V}{A \times P \times t} \tag{2}$$

where J (L·m^{-2}·h^{-1}) refers to the pure water flux, V (L) means the permeate water volume, A (cm^2) represents the effective filtration area, P (bar) is the operating pressure, and t (h) is the filtration time.

The porosity of the membrane was calculated using Eq. (3).

$$\varepsilon = \frac{m_w - m_d}{\rho_w Ad} \times 100\% \tag{3}$$

where m_w and m_d (g) represent the wet and dry membranes masses, respectively, ρ_w (g·cm^{-3}) refers to the pure water density, A (cm^2) represents the membrane area, and d (cm) means the thickness of membrane.

The HA rejection rate reflects the separation performance of the membrane for macromolecular contaminants and can be obtained by Eq. (4).

$$R = \frac{C_0 - C}{C_0} \times 100\% \tag{4}$$

where R is the rejection rate of HA, C_0 and C (mg·L^{-1}) represent the HA

concentration in the initial solution and the solution after membrane filtration, respectively. The concentration of HA was detected by the UV–vis spectroscope at 254 nm.

The flux recovery rate (*FRR*) is used to assess the anti-fouling performance of the membrane. Firstly, the membrane was pre-pressurized with deionized water at 0.15 MPa for 0.5 h, and subsequently reduced to 0.1 MPa to measure and record the initial pure water flux (J_0) of the membrane. Subsequently, the deionized water was substituted with the contaminant solution, and the flux of the contaminated membrane was calculated for 0.5 h. Then, the membrane was washed with a PMS solution at a concentration of 1.0 mM for 15 min, and the permeate flux of the cleaned membrane was measured and recorded (J_1). The above operation was repeated 3 times to obtain the FRR by Eq. (5).

$$FRR = \frac{J_1}{J_0} \times 100\% \tag{5}$$

The influence of various reaction conditions onto the catalytic degradation performance of the membranes was analyzed by comparative tests. Typically, 500 mL of 15 ppm TC solution was used as the target contaminant. After the cycle started, PMS were added to the solution. PMS was activated by contacting with the catalyst at the membrane surface and within the pores of the membrane, and the final degraded solution was run off through the membrane. At regular intervals, the TC concentration in the degraded solution was detected with the UV–vis spectroscope.

3. Results and discussion

3.1. Characterization of perovskite catalyst particles

The XRD of the prepared perovskite particles are shown in Fig. S2. It was observed that no A$_2$BO$_4$-type perovskite was formed by calcining the precursors at 850 °C without adding Sr at all. If Sr doping x < 40 % or x > 80 %, the calcination products showed a mixture of ABO$_3$ perovskite and A$_2$BO$_4$ perovskite. When the feeding molar ratios of La and Sr were close to each other (40 % ≤ x ≤ 60 %), the calcined oxide exhibited pure A$_2$BO$_4$ phase. Besides, the characteristic diffraction peak gradually shifted to a higher angle with the addition of Sr, indicating the success of incorporating Sr into the perovskite lattice [12]. Although the cation size of La^{3+} (1.32 Å) was smaller than that of Sr^{2+} (1.44 Å), the introduction of low-valent Sr^{2+} introduces more surface anionic defects such as oxygen vacancies to maintain the electrical neutrality of the material, which may lead to greater lattice shrinking [25]. Among them, the LSC50 perovskite possessed clearer and sharper characteristic peaks, so it was further evaluated.

As shown in Fig. 1(a), LSC50 exhibited an irregular bulk structure with particle size distribution ranging from tens to hundreds of nanometers. The catalyst surface was smooth and agglomeration was evident. As indicated in Fig. 1(b, c, d, e, f), the four elements La, Sr, Co and O were uniformly distributed and the atomic ratios of La, Sr, Co, and O were 13.18, 11.12, 11.77, and 63.93 %, respectively, which were approximately similar to the molar ratios of the feeds. From Fig. 1(g, h), it was observed that the TEM image of LSC50 possesses the same morphology as the SEM image. And the lattice stripe spacing of LSC50 catalyst is 0.274 nm, which corresponds to (110) crystal planes according to PDF# 97-009-9897 [38].

The XPS spectra for LSC50 catalyst are shown in Fig. 2. The signals of La, Sr, Co, and O were investigated. Co is generally considered to be the key element of PMS activation. Fig. 2(b) illustrated the Sr 3d spectrum of LSC50 catalyst. The fitted peaks located at ~132.1, ~133.7, and ~135.4 eV were attributed to Sr^{2+} in perovskite, surface oxide and carbonate, respectively [39]. As indicated in Fig. 2(c), the Co 2p spectrum of Co showed two main peaks at about 780.5 and 795.9 eV, which could be attributed to Co 2p$_{3/2}$ and Co 2p$_{1/2}$, respectively [22]. The fitted peaks at ~781.9 and ~797.1 eV were Co (II), while the fitted peaks at ~790.3 and ~795.4 eV were Co (III). In Fig. 2(d), three valent O
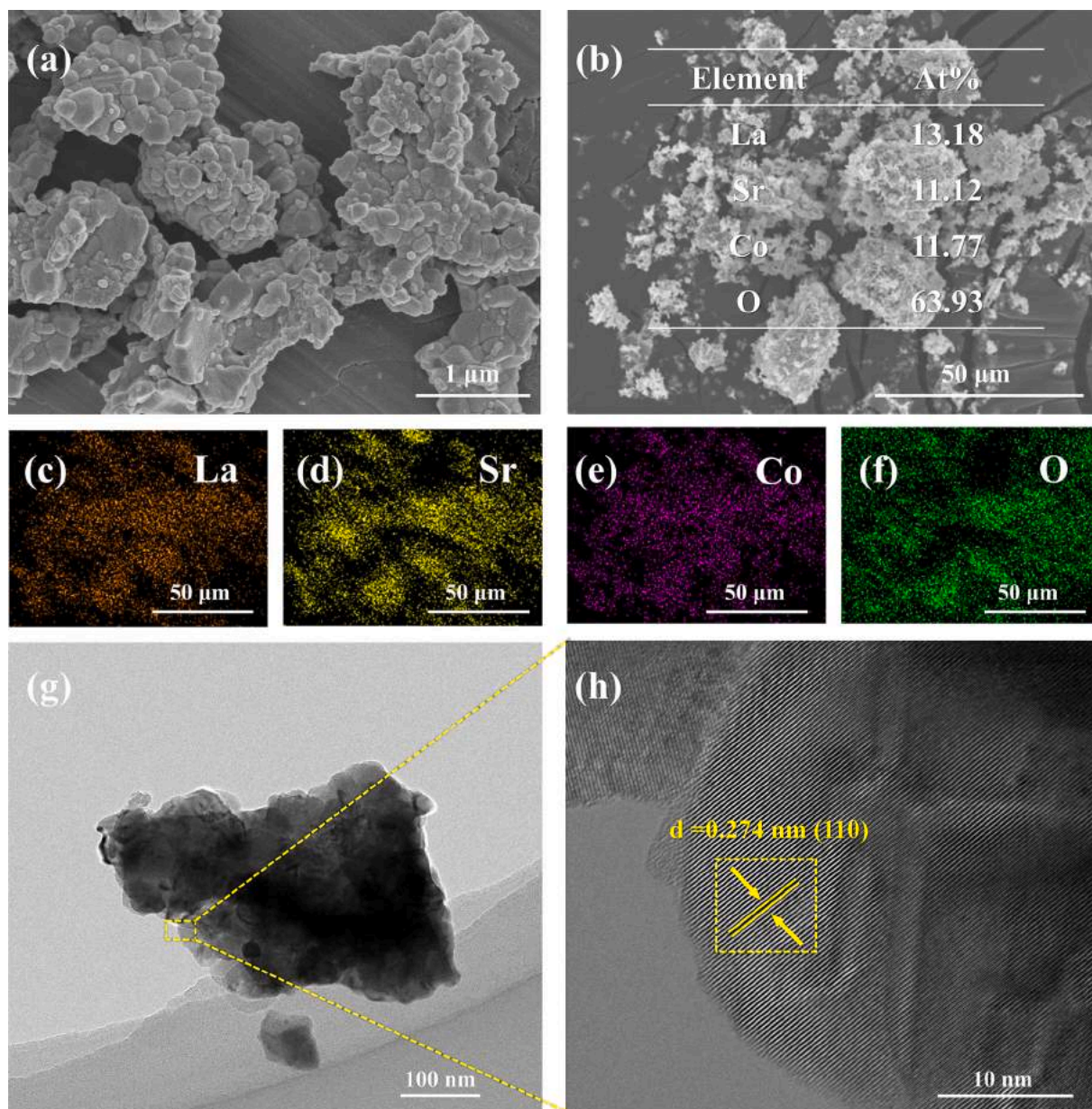
Fig. 1. SEM, EDS Mapping and TEM images of LSC50.

elements were present in the O 1 s spectrum, which were lattice oxygen (O_L), surface oxygen (O_A) and oxygen in water molecules (O_H). The fitted peaks localized at ~528.9, ~531.3 and ~ 533.0 eV correspond to the O_L, O_A and O_H, respectively [40]. Moreover, the XPS spectra of various perovskites were compared. As exhibited in Fig. S3(a), the peaks of A_2BO_4 perovskite were shifted slightly to the positive binding energy region in comparison with ABO_3 perovskite, suggesting that A_2BO_4 perovskite possessed a lower surface Co oxidation state compared to ABO_3. Among them, LSC50 exhibited the lowest Co oxidation state [21,22]. As shown in Fig. S3(b), the ratio of Co^{2+}/Co^{3+} in LSC50 was 0.44, higher than that of 0.35 for LCO. It is worth observing that the O_A/O_L ratio could to evaluate the relative content of oxygen vacancies in perovskite oxides [41].As indicated in Fig. S3(c, d, e, f, g), the O_A/O_L ratio of LSC50 was 5.53, higher than the other perovskite particles, indicating that more oxygen vacancies were generated in LSC50 structure. EPR analysis also indicated that the oxygen vacancy content of the LSC50 was higher than that of the ABO_3-type LSCO perovskite (Fig. S4).

3.2. Degradation performance of powder perovskite catalyst

In Fig. 3(a), the TC degradation ability of different perovskite particles was investigated. The catalysts were considered to reach TC adsorption/resolution equilibrium after 10 min by feeding 0.05 $g \cdot L^{-1}$ of perovskite particles into 15 ppm TC solution. The high forming temperature of the perovskite catalysts resulted in a low specific surface area (Fig. S5), so that all the prepared catalyst particles could adsorb only about 5 % TC. By adding 0.5 mmol PMS, the TC was gradually degraded. For the ABO_3 perovskite, the A-site Sr substitution slightly enhanced the degradation efficiency of the catalysts. Since the Co-based perovskite possessed high catalytic activity, the enhancement effect brought by Sr doping was not significant. In contrast, for A_2BO_4 perovskite, the effect brought by Sr doping was more obvious. Among them, LSC50 had the best catalytic ability and could completely degrade TC within 12 min, which may be attributed to the highest number of oxygen vacancies in LSC50. Meanwhile, the catalytic ability of A_2BO_4-type perovskites was better than ABO_3 perovskites. According to the kinetic analysis, as indicated in Fig. 3(b), the degradation of TC followed the pseudo-first-
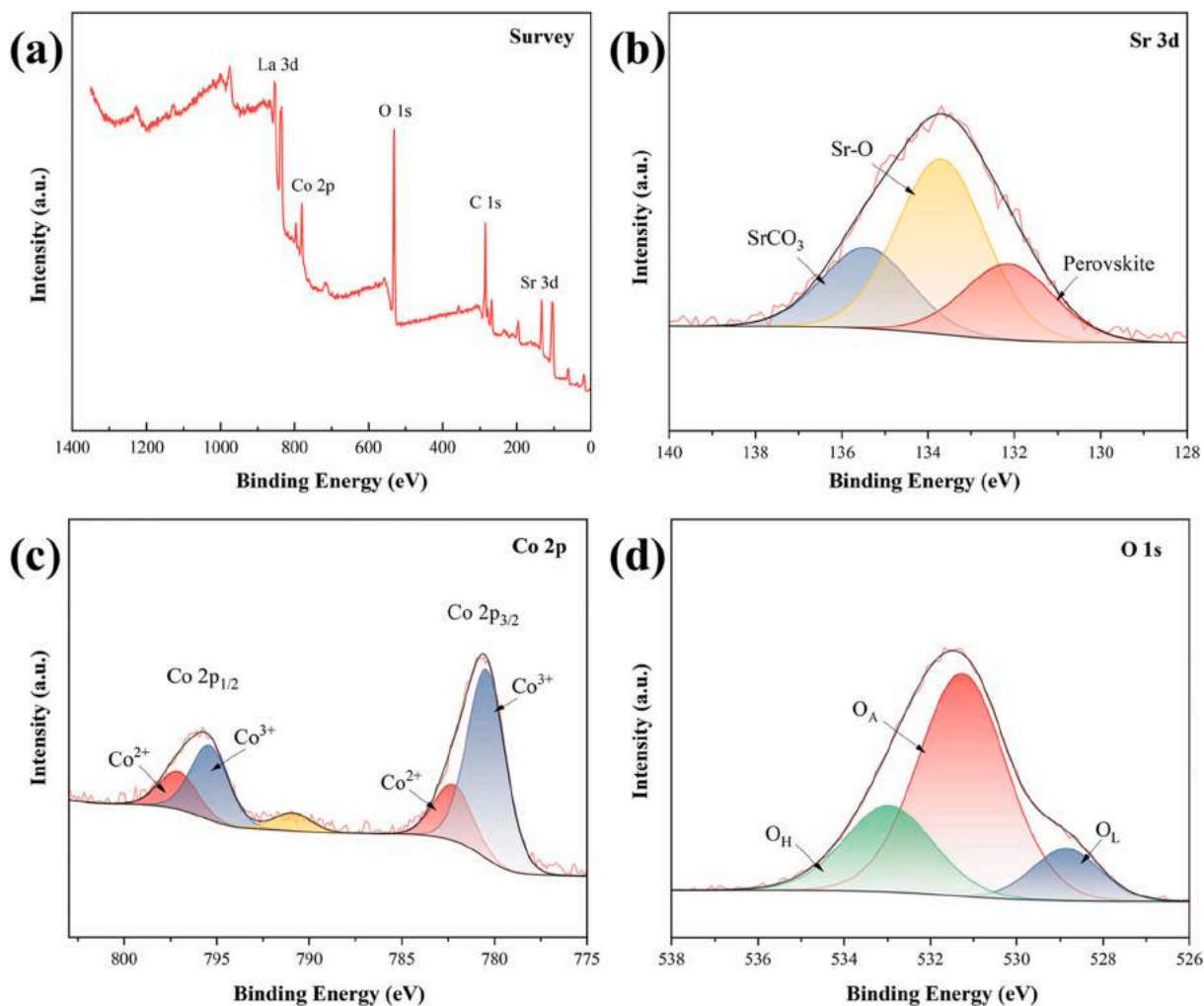
Fig. 2. XPS spectra of LSC50 perovskite (a), Sr 3d spectrum (b), Co 2p spectrum (c), and O 1 s spectrum (d).
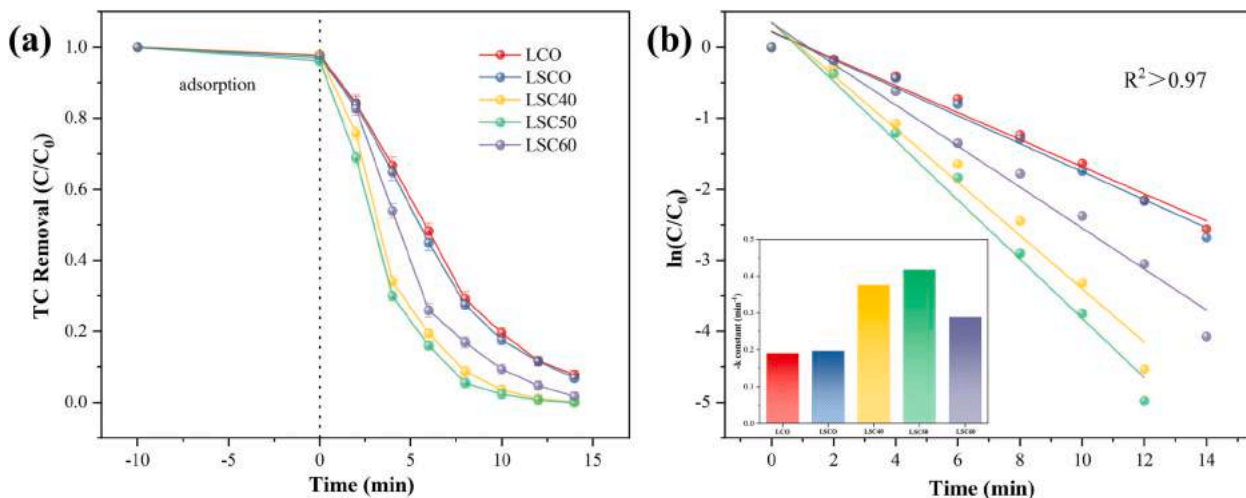
Fig. 3. Degradation curves of TC (a) and reaction rate constants k (b) by perovskite catalyst. Conditions: [TC] = 15 mg·L^{-1}, [PMS] = 0.5 mM, [catalyst] = 0.05 g·L^{-1}.

order kinetic equation. k value of LSC50 was calculated to be 0.4176 min^{-1}, which was 2.2 times that of LCO and 2.1 times that of LSCO. In conclusion, LSC50 was selected for the preparation of PAN/LSC-y catalytic separation membranes.

3.3. Structure and permeability of catalytic membrane

The cross-section and surface morphology of PAN and PAN/LSC-y catalytic membranes are indicated in Fig. 4. All membranes exhibited typical asymmetric structures consisting of a dense skin layer and porous
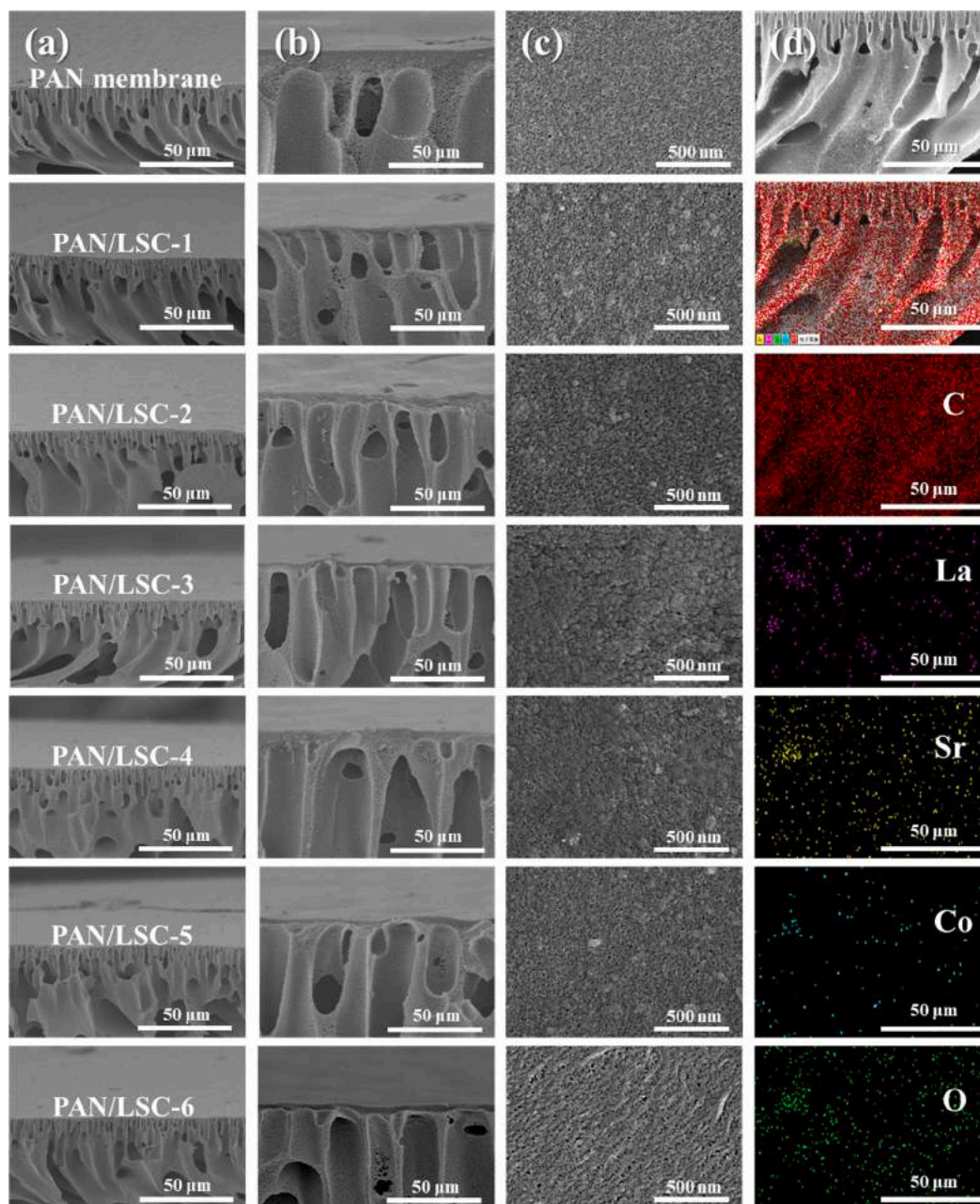
Fig. 4. SEM images of catalytic membranes with different LSC50 contents. (a) Cross-sectional structure, (b) magnified cross-sectional morphology, (c) surface morphology and (d) EDS image of catalytic membranes.

support layer with a finger-like structure, suggesting strong invasion of the PAN/NMP phase by non-solvents during membrane formation process. Fig. 4(a) exhibits that with the addition of LSC50, a greater number of micropores appeared in the membrane sublayer. And in Fig. 4(b), it appears that the epidermal layer of the catalytic membrane was less thick than the initial PAN membrane. These structural changes are due to the addition of LSC50 particles, which increased the viscosity of the casting solution, thereby impeding the fluidity of the polymer chains, prolonging the phase transition process, and thus increasing the porosity. As shown in Table S1, the average pore size in PAN membranes was 17.97 nm. The average pore size of the membranes increased and then decreased with the addition of LSC50, and the PAN/LSC-4 membrane had the highest pore size (27.53 nm). As a result, the water permeability of the catalytic membrane was significantly increased, the resistance to mass transfer was greatly reduced [37,42]. However, when 6 wt% of LSC50 was introduced into the membrane, as exhibited in

Fig. 4(c), obvious wrinkles were detected on the membrane surface, indicating that the viscosity of the casting solution was extremely high. This might lead to decreased porosity and increased densification of the membrane, which negatively affected the permeability performance of the membrane [43]. Besides, as indicated in Fig. 4(d), the EDS mapping showed that the LSC50 was embedded uniformly in the surface and pores of the membrane. Table S2 lists the elemental composition of PAN/LSC-5 catalytic membranes, which shows that LSC is successfully incorporated into PAN membranes.

To evaluate the membrane permeation performance, the pure water flux of the membrane was tested. As depicted in Fig. 5(a), with the addition of LSC, the pure water flux of the membrane showed a tendency to increase and then decrease, reaching a peak value of 1086.1 $L \cdot m^{-2} \cdot h^{-1}$ at a concentration of 5 wt% LSC50. A similar trend was also observed for porosity. These results are consistent with speculation in previous SEM analysis results. The hydrophilicity of the membrane was
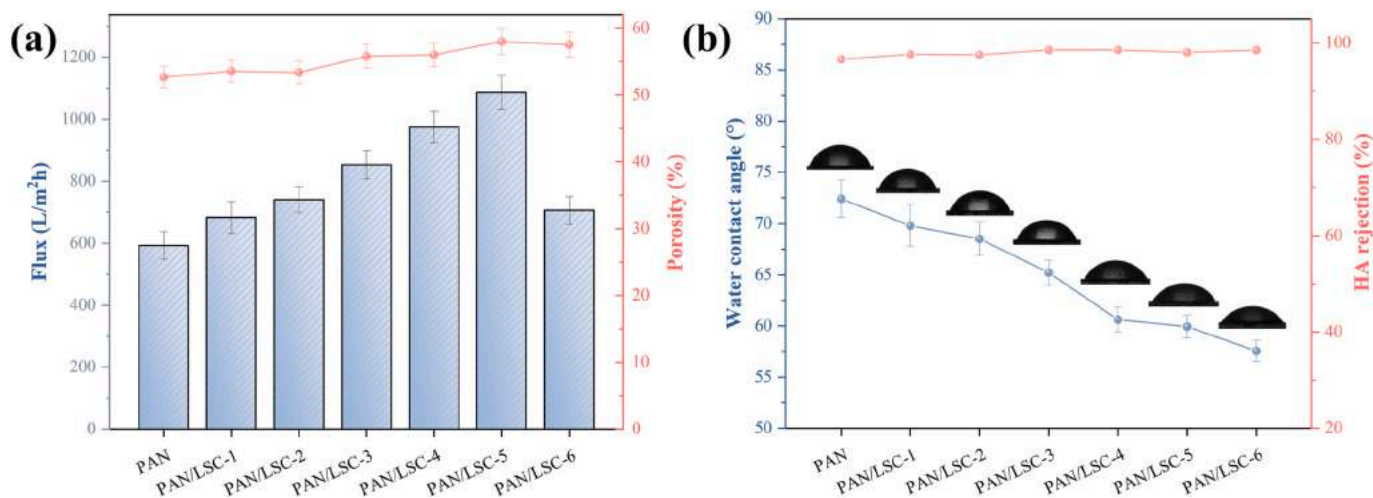
Fig. 5. (a) Pure water flux and porosity, and (b) water contact angle and HA inhibition performance.

characterized by measuring the water contact angle. From Fig. 5(b), it can be observed that as the mass of LSC50 particles embedded in the membrane matrix increases, the water contact angle of the membrane decreases. This indicates that the introduction of hydrophilic LSC50 catalyst particles improves the hydrophilicity of PAN membranes. The ability of membranes to reject large molecular contaminants was further investigated using HA as a contaminant. In Fig. 5(b), it can be found that all membranes possess good HA retention, which provides a prerequisite for effective synergism between the separation and degradation performance of catalytic membranes.

3.4. Degradation performance of catalytic membranes

By coupling the AOPs with membrane separation, the resulting PAN/LSC catalytic membranes exhibited excellent TC degradation performance. The degradation performance of the catalytic membranes was assessed by the TC removal efficiency, and the results are presented in Fig. 6(a). The original PAN membrane was able to remove about 29.7 % of TC in 30 min without the addition of PMS, because of the porous structure of the polymer membrane that allows the membrane to partially adsorb the TC. After the addition of PMS, the removal of TC by the PAN membrane was increased to 67.2 % in 30 min. This improvement in catalytic performance was primarily due to a significant increase in the local PMS and contaminant concentration within the confines of the membrane pore channel, which allowed rapid generation of ROS in the membrane structure [35,37,44]. Apparently, the degradation efficiency of TC by catalytic membranes increased continuously with the increase of LSC50 content. It is noteworthy that PAN/LSC-5 membranes can remove >90 % of TC within 3 min and reach a removal rate above 99 % within 27 min, reflecting excellent degradation rate. The filtrate after 30 min of degradation reaction was tested and both UV and liquid chromatography results showed that the TC was removed (Fig. S6). Interestingly, when the LSC50 content in the catalytic membrane exceeded 2 wt%, the short-time degradation rate of the catalytic membrane was higher than that of the LSC50 catalyst particles. This is due to the uniform distribution of the LSC50 catalyst in the PAN/LSC membrane, which provides better dispersion compared to the LSC50 powder. Moreover, the membrane pores served to enhance the mass transfer and mitigate the limitation caused by the low specific surface area of LSC50. Besides, there was no significant increase in the degradation rate of PAN/LSC-6 membrane compared to PAN/LSC-5 membrane. Thus, considering the results of the previous pure water flux test, the PAN/LSC-5 membrane was selected for the subsequent study.

3.5. Effect of operating conditions

The effect of different parameters on the degradability of the PAN/LSC-5 membrane was investigated. The degradation performance of catalytic membranes was tested at 25, 35, and 45 °C, and the results are presented in Fig. 6(b). A number of studies suggested that the higher temperature accelerated the breaking of the -O-O- bond in PMS and accelerated the generation of ROS [45]. Nevertheless, there was only a 1.9 % increase in TC removal with a 20 °C increase in temperature. On the basis of the Arrhenius equation ($\ln k = -Ea/RT + \ln A$), we suggest that PAN/LSC catalytic membranes can significantly reduce the activation energy of the reaction (Ea) for PMS activation, which not only facilitates the removal of organic pollutants, but also reduces the energy consumption during the reaction.

The pH of the solution has a significant effect on the degradation performance of the catalytic membrane as it affects the generation of free radicals. The test results at varied pH are shown in Fig. 6(c). Within 30 min, the vast majority of TC was degraded at pH values of 5, 7 and 9. This is because PMS has a pK_{a2} of 9.4, the major form of PMS present when the pH of the solution is 5–9 is HSO_5^-, which favors the further production of the highly reactive $SO_4^{\bullet-}$ and $^1O_2$ [46]. On the other hand, while the pH was 3 and 11, the removal rate of TC decreased to 75.2 % and 85.7 %, respectively. This is because at when the pH is <3, the formation of $CoOH^+$, an important intermediate leading to $SO_4^{\bullet-}$ production, is suppressed [47]. In addition, excess H^+ reacts with $SO_4^{\bullet-}$ and ·OH, resulting in the depletion of ROS. Furthermore, at a pH above 9, the major form of PMS is converted to SO_5^{2-}, which is less active than $SO_4^{\bullet-}$ [45]. At pH above 10, $SO_4^{\bullet-}$ reacts with OH^- and generates ·OH, which has a weaker oxidation capacity compared to $SO_4^{\bullet-}$ [48]. This means that the catalytic membrane can rapidly degrade TC in neutral conditions as well as in weakly acidic and weakly alkaline conditions. Meanwhile, since PMS is an acidic oxide, the solution pH decreases and remains to about 5–6 after the addition of PMS, and thus the initial pH of the solution was not adjusted for the subsequent experiments.

Under the above operating conditions, the impact of PMS content on the catalytic degradation effect of the membrane was investigated. As shown in Fig. 6(d), the TC removal rate of the catalytic membrane decreased when the PMS was 0.25 mmol. And due to the low content of ROS, when the adsorption of TC by the membrane reached equilibrium, part of the undegraded TC would enter the filtrate, resulting in a temporary increase of TC content within 5–10 min [32]. In addition, the improvement brought by high PMS content was not obvious when the PMS content was higher than 0.5 mmol. Therefore, 0.5 mmol was considered the most appropriate PMS concentration. One possible explanation for this phenomenon is that the local PMS concentration is
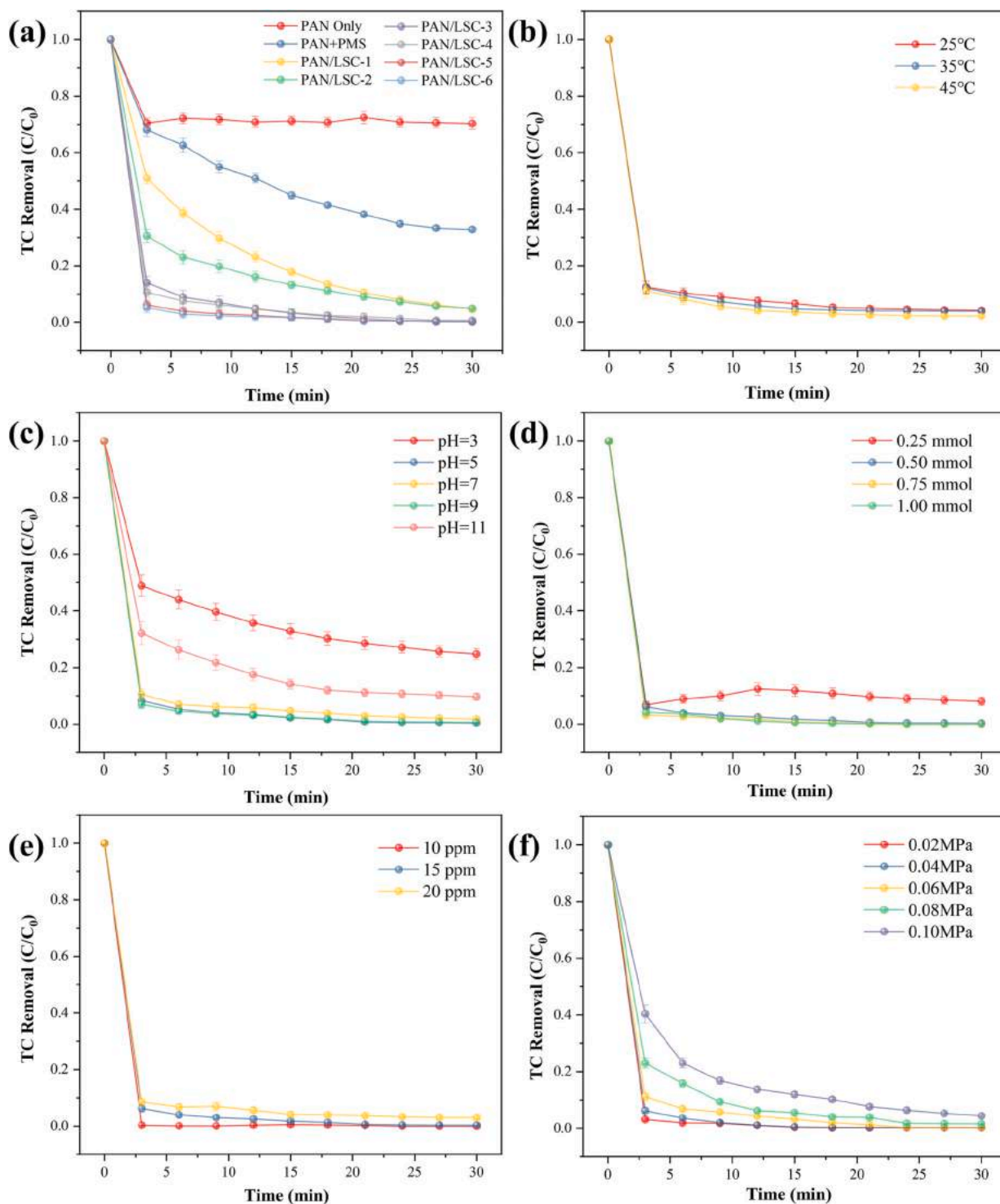
Fig. 6. (a) Degradation performance of catalytic membranes and effect of (b) temperature, (c) solution pH, (d) PMS addition, (e) TC concentration and (f) operating pressure on catalytic membrane. Conditions: [PMS] = 0.5 mM, [TC concentration]: 15 ppm, 500 mL, [effective membrane area] = 7.0 cm^2, [temperature] = 25 °C.

excessively high due to the increased mass transfer effect of membrane pores, which triggers ROS self-quenching [49]. Moreover, the effect of TC concentration on the membrane degradation performance was evaluated. As depicted in Fig. 6(e), the removal rate decreased with increasing TC concentration. When the concentration of TC was 15 ppm and 20 ppm respectively, 99.6 % and 97.0 % of the pollutants were degraded. Of note, the PAN/LSC-5 membrane was able to remove 99.7 % of the contaminants in <3 min when the TC concentration was 10 ppm. This indicates that the catalytic membrane has an excellent

degradation efficiency for TC.

Fig. 6(f) represents the relationship between the operating pressure and degradation performance. The pure water flux and residence time (*T*) of the catalytic membrane at different operating pressures are shown in Table 1 (*T = d/F*). As the pressure increased, the degradation rate of TC by the membrane gradually decreased, which was caused by both the higher accumulation rate of the pollutants and the shorter residence time of the pollutants in the membrane. At a pressure of 0.1 MPa, only about 60 % of the TC was removed in the first three minutes, while the

Table 1
Permeation flux of the PAN/LSC-5 membrane toward TC aqueous solution under various operating pressures.

Pressure (MPa)	0.02	0.04	0.06	0.08	0.10
Flux (L·m^{-2}·h^{-1})	157.8	386.9	557.5	702.1	788.5
Retention time (s)	2.27	0.93	0.64	0.51	0.45

TC removal rate reached 97 % in three minutes when the pressure was reduced to 0.02 MPa. In addition to contributing to lower operating costs, the lower operating pressure had exhibited a positive effect on TC degradation. Besides, to further evaluate the rate of TC mineralization by the catalytic membrane, the TOC of the treated solution was investigated at different processes. As shown in Fig. S7, approximately 62.1 % of the TC was mineralized into CO_2 and H_2O after 3 consecutive operating processes. In summary, the PAN/LSC-5 catalytic membrane had an excellent degradation effect on TC and could be adapted to a variety of operating environments.

3.6. Influence of environmental factors on catalytic membrane performance

The presence of various inorganic anions and NOM may affect the activation process of PMS by inhibiting electron transfer progress. Therefore, it is necessary to evaluate these influencing factors. As presented in Fig. 7(a), the introduction of anions inhibited the degradation of TC to varying degrees, which possibly attributed to the anions reacting with ROS or occupying the active site of the reaction [50]. In particular, $H_2PO_4^-$ displayed the most pronounced inhibition, reducing the degradation rate of TC to 91.3 %, while Cl^-, HCO_3^-, and NO_3^- showed a slight inhibitory effect on TC degradation. This suggests that PAN/LSC catalytic membranes can maintain favorable TC degradation efficiency in coexistence with inorganic anions. To further verify the ability of the membrane to purify complex wastewater, different concentrations of HA and 15 ppm of TC were complexed and treated as target pollutants. In principle, HA, as a naturally occurring organic macromolecular compound, can effectively limit the generation of ROS. Due to the sieving effect of the membrane, HA cannot pass through the membrane and is rejected to the outside of the membrane, while TC penetrates the membrane and can be degraded in the channel-assisted reaction sites. As illustrated in Fig. 7(b), the membrane can degrade 98.9 % of TC in <30 min even when the HA content is 200 ppm, which demonstrates the efficient synergy between membrane separation and degradation. Accordingly, to evaluate the potential of catalytic membranes in practical applications, TC degradation tests were performed using different water matrices. As depicted in Fig. 7(c), the catalytic membrane could realize high TC degradation in both tap water and river water, and the degradation rate slightly reduced. In conclusion, the PAN/LSC-5

catalytic membranes exhibited considerable adaptability to different effluents.

3.7. Stability, recyclability and anti-fouling properties of catalytic membranes

Well-stability and repeatability are the guarantees that the catalytic membrane can be applied to practical operation. Fig. 8(a) shows the repeatability test of the PAN/LSC-5 catalytic membrane. After 5 cycles, the membrane can still achieve a TC removal rate of 98.7 % in 30 min, demonstrating high stability. On the other hand, the catalytic efficiency of the membrane decreased, possibly due to the increased oxidation state of the transition metal ions in the LSC50 particles or due to the depletion of reactive oxygen species, which affected the continuation of the non-radical pathway [22].

The leaching of cobalt ions has been an important factor limiting the development of cobalt-based catalysts. The tortuous channels of the catalytic membrane greatly enhance the mass transfer efficiency of the oxidation reaction, and the contaminants are rapidly degraded within a short residence time. The shortened residence time ensures the stability of the LSC50 catalysts to a certain extent [37]. Table 2 shows the metal ion leaching from the catalytic membrane in 1, 3 and 5 cycles. The cobalt ion leaching from the catalytic membranes is significantly lower than the Chinese wastewater discharge standard (GB-25467-2010, ≤1 mg/L), reflecting an excellent environmental friendliness. In addition, the leaching of strontium ions was slightly higher than that of lanthanum and cobalt, which may indicate the poor stability of the strontium element present in the surface oxides of the catalysts.

In order to evaluate the membrane antifouling performance, a simulated wastewater containing 15 mg·L^{-1} TC and 100 mg·L^{-1} HA as target pollutants was used to compare the recovery of membrane flux from the original PAN membrane and the catalytic membrane after cleaning with PMS. As depicted in Fig. 8(b), the solution flux of PAN and catalytic membranes decreased significantly after the addition of pollutants compared to pure water, indicating that the deposition of pollutants resulted in severe membrane fouling. Based on the catalytic degradation characteristics of the catalytic membrane, the accumulated contaminants on the membrane surface and in the pore could be effectively removed by catalytic oxidation. After three consecutive contamination cleaning cycle operations, the flux recovery rate of PAN/LSC-5 catalytic membrane was 71.3 %, which is significantly higher than 28.5 % of the original PAN membrane, proving that the catalytic membrane has good long-term anti-fouling performance.

3.8. Analysis of the degradation mechanism of catalytic membrane

Generally, in the AOPs, PMS is activated to ROS with strong
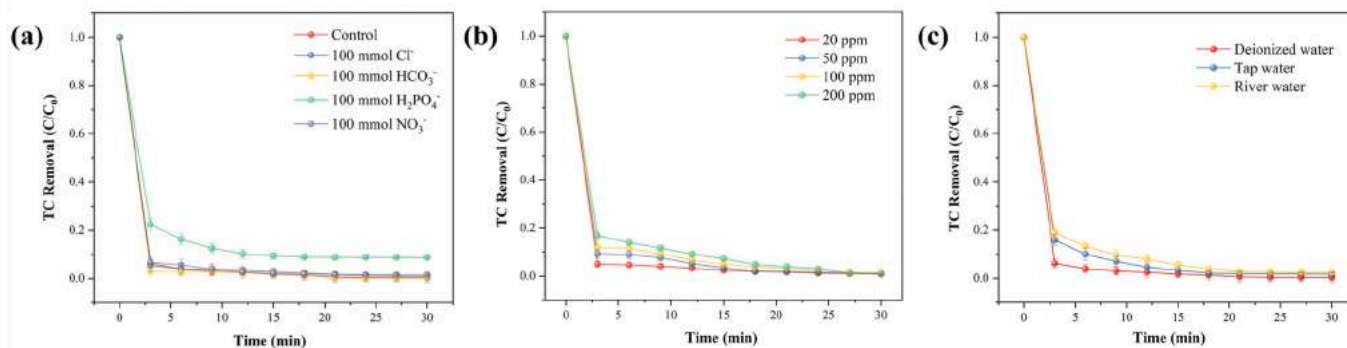
Fig. 7. Effect of (a) inorganic anion, (b) HA addition, and (c) aqueous substrate on the degradation performance of catalytic membranes. Conditions: [PMS] = 0.5 mM, [TC concentration]: 15 ppm, 500 mL, [effective membrane area] = 7.0 cm^2, [temperature] = 25 °C.
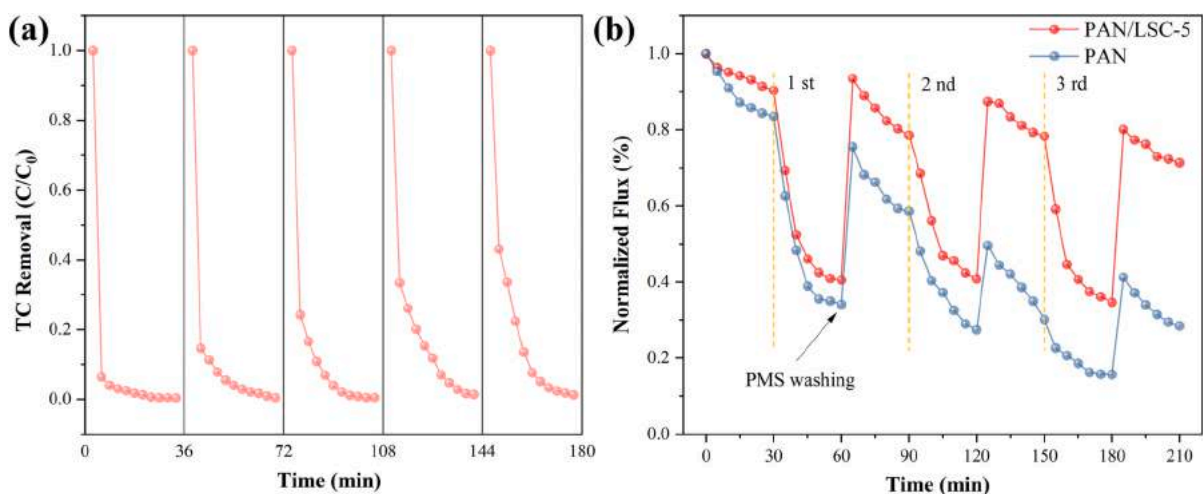
Fig. 8. (a) Cycling stability and (b) anti-fouling properties of catalytic membranes.

Table 2
Metal leaching of catalytic membrane during each run.

Cycles	Metal leaching during reaction		
	La $(mg·L^{-1})$	Sr $(mg·L^{-1})$	Co $(mg·L^{-1})$
1 st	0.03314	0.09779	0.01274
3 rd	0.04623	0.09566	0.00688
5 th	0.03800	0.10139	0.00840

oxidizing power and achieves further degradation of organic pollutants. As typical ROS, hydroxyl radicals (·OH) and sulfate ($SO_4^{•-}$) are radicals, while singlet oxygen ($^1O_2$) is non-radical. In order to determine the types of ROS in the present experiments, quenching experiments are performed. TBA, MeOH and FFA were selected to quench ·OH, $SO_4^{•-}$ and $^1O_2$, respectively [51,52]. As depicted in Fig. 9(a), the addition of 0.2 mol·L^{-1} TBA exhibited only a weak inhibitory effect on the degradation of TC. In contrast, the removal rate of TC was reduced to 47.5 % in <30 min following the addition of 0.2 mol·L^{-1} MeOH. Both TBA and MeOH were reported to be effective at quenching ·OH, but the reactivity of MeOH containing α-hydrogen toward $SO_4^{•-}$ is much greater than the TBA without α-hydrogen [53]. Therefore, the correlation results indicated that $SO_4^{•-}$ dominated in the free radical pathway. For the non-free pathway, the removal of TC was reduced to 33.4 % in the presence of 0.01 mol·L^{-1} of FFA, which had a stronger inhibitory effect than 0.2 mol·L^{-1} of MeOH. These results suggested that, apart from free radicals, a large amount of $^1O_2$ was generated during the reaction, and this non-free radical pathway played a critical role in the TC degradation process. This is similar to the conclusion reached in the study of Li et al.

concerning the degradation of phenol by RP-type perovskite [22]. To develop further evidence for the presence of free radical and non-free radical pathways in the TC degradation process, EPR analysis with DMPO and TEMP as spin-trapping agents revealed the generation of ·OH, $SO_4^{•-}$ and $^1O_2$. As in Fig. 9(b), the characteristic peaks of DMPO-·OH and DMPO-$SO_4^{•-}$ adducts were observed at both the 15th min and 30th min of the reaction, indicating the formation of $SO_4^{•-}$ and ·OH. However, the lower peak values of the obtained characteristic EPR signal peaks may indicate that the system contains a less amount of $SO_4^{•-}$ and ·OH species. Moreover, the typical three-line EPR spectrum of apparent TEMP-$^1O_2$ is shown in Fig. 9(c), confirming the generation of $^1O_2$.

According to previous considerations, the LSC50 perovskite activation of PMS for TC degradation is a coexistence of free radical pathways and non-radical pathways. In order to investigate the active sites as well as the valence changes of the metal elements during the reaction, the XPS spectra of LSC50 particles before and after the reaction were evaluated. As Fig. 10(a), in the Co 2p XPS spectrum, the Co^{2+}/Co^{3+} ratio decreased from 0.44 to 0.25, illustrating the presence of an active redox cycle. For the O 1 s spectrum, as shown in Fig. 10(b), the ratio of surface oxygen to lattice oxygen (O_A/O_L) decreased from 5.53 to 4.29, reflecting the involvement of oxygen vacancies as active sites in the reaction process. The surface hydroxyl (O_H) increased from 23.8 % to 29.5 %, which is probably due to the adsorption of intermediates in the reaction [54]. Additionally, Fig. 10(c) presents the Sr 3d XPS spectrum in which the ratio of $SrCO_3$ to Sr in the perovskite structure varies only slightly (from 1.0 to 1.1), while the Sr in the surface oxide shows a significant decrease. This may be caused by the possibility that the Sr in the surface oxide (Sr-O) is unstable and therefore leaches into solution during the reaction, consistent with previous speculations.
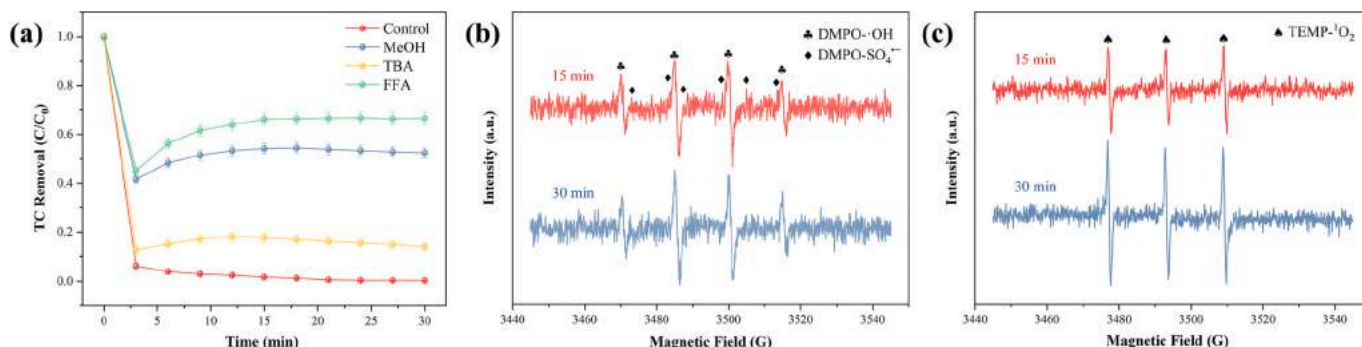
Fig. 9. (a) Radical quenching test, (b) EPR analysis of $SO_4^{•-}$ and ·OH, (c) EPR analysis of $^1O_2$.
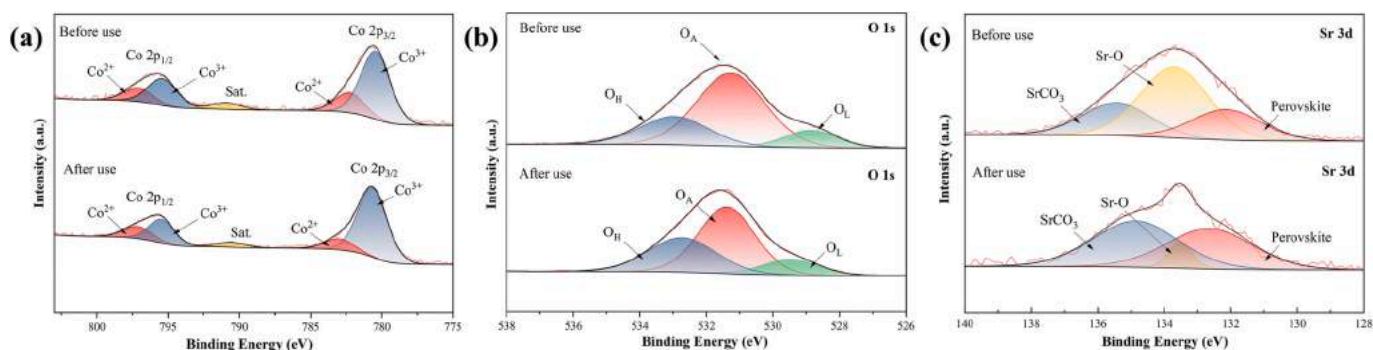
Fig. 10. Comparison of (a) Co 2p spectrum, (b) O 1s spectrum, and (c) Sr 3d spectrum before and after the reaction of LSC50 perovskite.

Based on the above analysis, a possible reaction mechanism for the activation of PMS by the catalytic membrane was postulated. First, through Eq. (6), accompanied by the redox reaction of Co^{3+}/Co^{2+}, the PMS coupled with the lattice oxygen (O_O^X) in the LSC to produce oxygen vacancies ($V_O^{\bullet}$) and part of $^1O_2$. The Co^{3+}/Co^{2+} redox is more active than the Co^{4+}/Co^{3+} redox. The Co element valence in the RP perovskite is closer to 3 and consequently more susceptible to $^1O_2$ generation than the ABO_3 perovskite [55]. According to Eq. (7), PMS radical ($SO_5^{\bullet-}$), which has a low redox potential, is also generated during the redox of Co^{3+}/Co^{2+}, and the undesirable redox ability of $SO_5^{\bullet-}$ contributed negligibly to the degradation of TC [56]. The consumption of lattice oxygen during the reaction invariably resulted in the forming of oxygen vacancies as intermediates, which together with the oxygen vacancies intrinsic to the perovskite structure, promoted the formation of free radicals $SO_4^{\bullet-}$ and ·OH via Eq. (8) and Eq. (9). Furthermore, these processes are accompanied by Co^{2+}/Co^{3+} redox reactions, thus enabling the redox cycling of Co ions. Meanwhile, the processes are also accompanied by the regeneration of lattice oxygen, which could continuously

promote the coupling of PMS with lattice oxygen through Eq. (6) since the lattice oxygen in RP perovskite is unstable. Notably, the RP perovskite structure has a unique highly reactive interstitial oxygen (O_i''), hence PMS can directly generate $^1O_2$ by coupling with the interstitial oxygen via Eq. (10). This possibility is more helpful for the non-radical pathway because it does not lead to the generation of $SO_4^{\bullet-}$ and ·OH by generating oxygen vacancies through Eq. (8) and Eq. (9). Besides, due to the high activity of the interstitial oxygen, the mobility of the oxygen in the perovskite was significantly enhanced, which rapidly replenished the interstitial oxygen consumed by the reaction and made the process of Eq. (10) sustainable [22]. In summary, the free radicals $SO_4^{\bullet-}$ and ·OH as well as the non-free radical $^1O_2$ interact synergistically through Eq. (11), which led to the deep degradation of TC and eventual mineralization into CO_2 and H_2O.

$$Co^{3+} + HSO_5^- + O_O^X \rightarrow Co^{2+} + HSO_4^- + {}^1O_2 + V_O^{\cdot\cdot} \tag{6}$$

$$Co^{3+} + HSO_5^- + H^+ + O_O^X \rightarrow Co^{2+} + SO_5^{\bullet-} + H_2O + V_O^{\cdot\cdot} \tag{7}$$
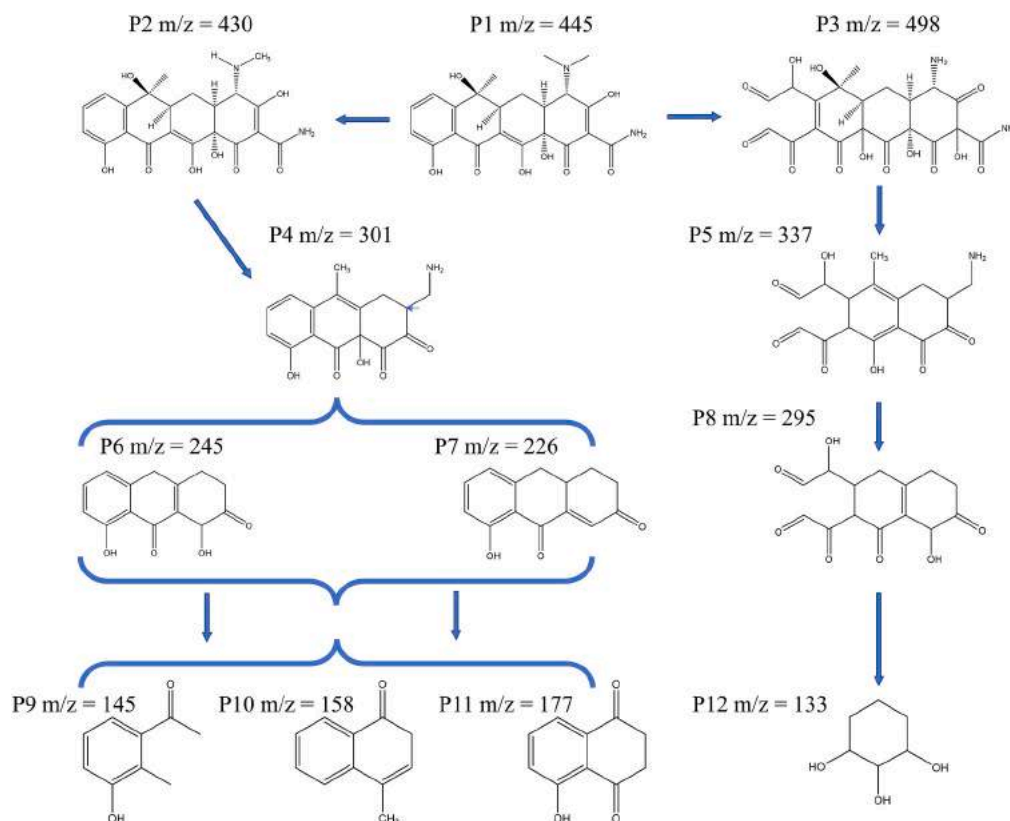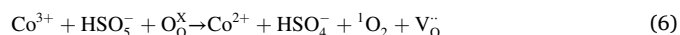
Fig. 11. Possible TC degradation pathways after catalytic membrane treatment.

$$Co^{2+} + HSO_5^- + V_O^{\cdot\cdot} \rightarrow Co^{3+} + SO_4^{\bullet-} + H^+ + O_O^X \tag{8}$$

$$Co^{2+} + HSO_5^- + H_2O + V_O^{\cdot\cdot} \rightarrow Co^{3+} + SO_4^{2-} + 2H^+ + \cdot OH + O_O^X \tag{9}$$

$$Co^{3+} + HSO_5^- + O_i^{\prime\prime} \rightarrow Co^{2+} + HSO_4^- + {}^1O_2 \tag{10}$$

$${}^1O_2 + SO_4^{\bullet-} + \cdot OH + TC \rightarrow Intermediates \rightarrow SO_4^{2-} + H_2O + CO_2 \tag{11}$$
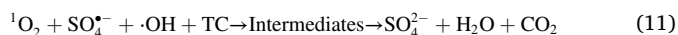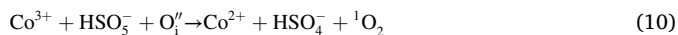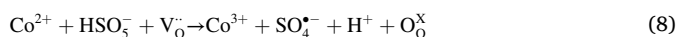
As illustrated in Fig. S8, the degradation intermediates of TC were analyzed by HPLC-MS. And the possible degradation routes of PAN/LSC membranes to TC were speculated. The possible degradation paths were analyzed as shown in Fig. 11. Under the attack of ROS, TC was oxidized to 2 possible intermediates P2 (m/z = 430) and P3 (m/z = 498) after demethylation, ring opening, decarbonylation and dehydroxylation reactions. Therefore, two possible pathways for TC degradation are postulated. In the first pathway, P2 was further oxidized to form P4 (m/z = 301). On this basis, P4 removed the alkyl and amino groups from the side chain to form P6 (m/z = 245) and P7 (m/z = 226), and further degraded to lower molecular organic compounds including P9 (m/z = 149), P10 (m/z = 158), and P11 (m/z = 177). In the second pathway, P3 opened the ring to form P5 (m/z = 337), then P5 removed the side chains to give P8 (m/z = 295), and P8 was further oxidized to P12 (m/z = 133). Eventually, P9, P10, P11, and P12 were completely mineralized to CO₂ and H₂O.

In order to investigate the environmental and biological effects of TC degradation process, the Toxicity Estimation Software Tool (T.E.S.T) with Quantitative Structure-Activity Relationship (QSAR) prediction was used to predict the developmental toxicity, mutagenicity, daphnia LC50 and oral rat LD50 of TC and its intermediates. Fig. 12(a) depicts the developmental toxicity of the intermediates, which were lower than

TC except for P7 and P8. Fig. 12(b) demonstrates the mutagenicity of the intermediates. TC was positive, and the mutagenicity of the intermediates tended to decrease as the reaction progressed, and more than half of the intermediates were negative. As shown in Fig. 12(c, d), the biotoxicity of the intermediates was significantly reduced after the catalytic membrane treatment. The toxicity of daphnia LC50 was attenuated from highly toxic to low toxic or even harmless, while the toxicity of oral rat LD50 was gradually reduced from toxic to harmful. In summary, the toxicity of degradation products was less than that of TC. Besides, compared with the separation and degradation capabilities of various catalytic membranes summarized in Table S3, PAN/LSC membranes exhibit desirable performance.

4. Conclusion

In this paper, A₂BO₄-type perovskite LSCx with Sr doping at the A-site was synthesized by simple sol-gel method. Compared with ABO₃ perovskite, the k constant of TC degradation by LSC50 was improved by >2 times, demonstrating excellent catalytic activity. Then, the LSC50 catalyst was embedded into the PAN membrane matrix by the phase conversion method to form PAN/LSC catalytic separation membrane. By confining contaminants and ROS within the membrane pores to enhance mass transfer, rapid regeneration of organic wastewater was achieved. The PAN/LSC-5 membrane was able to degrade 94 % of TC within 3 min and was adaptable to a variety of operating conditions with >24 % improvement over perovskite powder. Radical quenching experiments and EPR analysis indicated that $SO_4^{\bullet-}$ and ${}^1O_2$ played a dominant role in the catalytic oxidation. Meanwhile, these ROS effectively degrade the contaminants attached to the membrane surface, which imparts self-cleaning properties to the membrane. In addition, the PAN/LSC
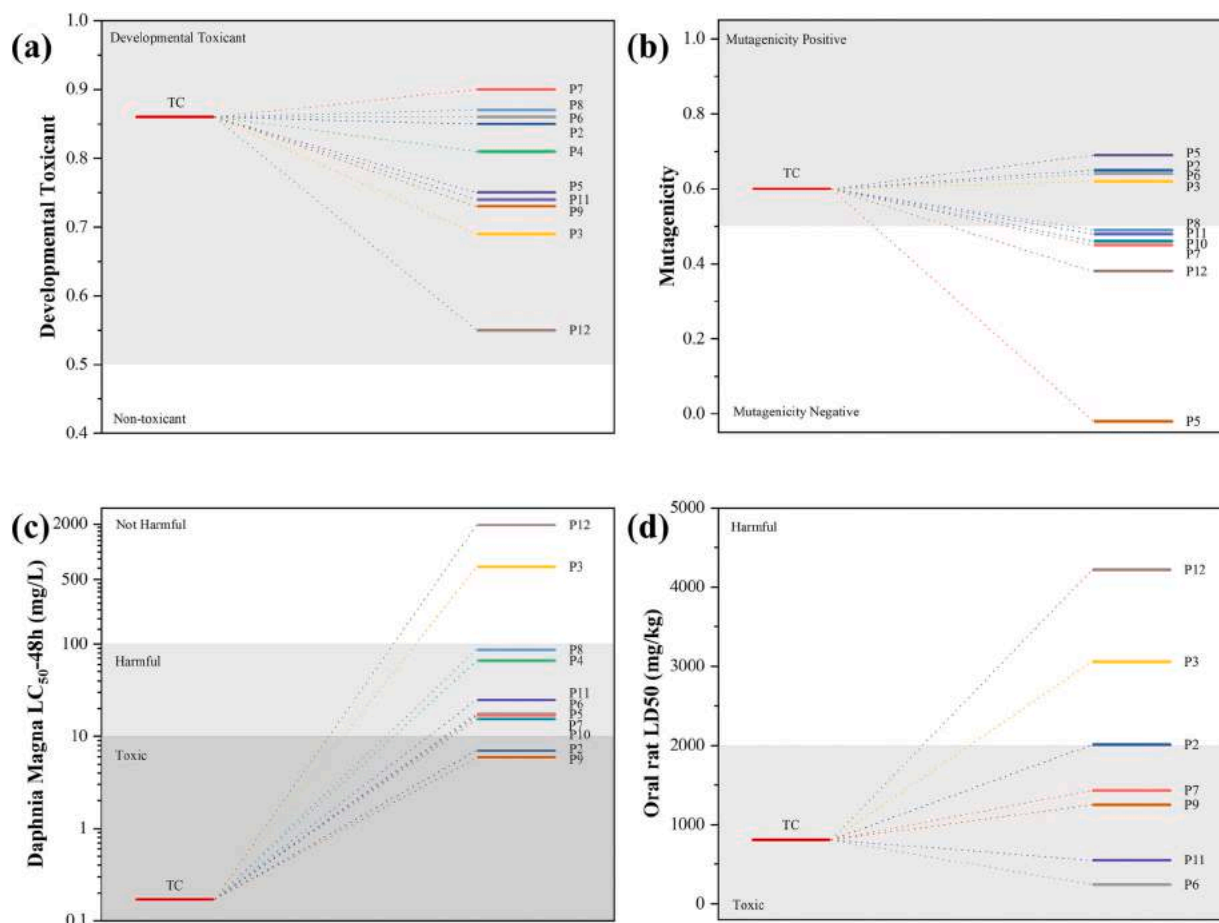
Fig. 12. Toxicity analysis of TC and degraded intermediates. (a) Developmental toxicity, (b) mutagenicity, (c) *daphnia magna* LC50, and (d) oral rat LD50.

membrane exhibited good cycling stability and lower ion leaching. The biological toxicity of the TC wastewater treated by the membrane was significantly reduced, reflecting a broad application prospect.

CRediT authorship contribution statement

Jingchao Yu: Investigation, Data curation, Writing – original draft. **Bin Jiang:** Data curation, Investigation, Methodology. **Longfei Zhang:** Data curation, Investigation, Methodology. **Yongli Sun:** Investigation, Methodology. **Luhong Zhang:** Investigation, Methodology. **Na Yang:** Conceptualization, Methodology, Project administration, Supervision, Writing – review & editing.

Declaration of competing interest

The authors declare that they have no known competing financial interests or personal relationships that could have appeared to influence the work reported in this paper.

Data availability

Data will be made available on request.

Appendix A. Supplementary data

Supplementary data to this article can be found online at https://doi.org/10.1016/j.jwpe.2023.103804.

References

[1] Z. Wang, H. Tang, W. Li, J. Li, R. Xu, K. Zhang, G. He, P.R. Shearing, D.J.L. Brett, Core–shell $TiO_2@C$ ultralong nanotubes with enhanced adsorption of antibiotics, J. Mater. Chem. A 7 (32) (2019) 19081–19086, https://doi.org/10.1039/c9ta06735c.

[2] L. Wang, A. Hu, H. Liu, K. Yu, S. Wang, X. Deng, D. Huang, Degradation of tetracycline hydrochloride (TCH) by active photocatalyst rich in oxygen vacancies: performance, transformation product and mechanism, Appl. Surf. Sci. 589 (2022), 152902, https://doi.org/10.1016/j.apsusc.2022.152902.

[3] C. Zhou, Y. Liang, W. Xia, E. Almatrafi, B. Song, Z. Wang, Y. Zeng, Y. Yang, Y. Shang, C. Wang, G. Zeng, Single atom Mn anchored on N-doped porous carbon derived from spirulina for catalyzed peroxymonosulfate to degradation of emerging organic pollutants, J. Hazard. Mater. 441 (2023), 129871, https://doi.org/10.1016/j.jhazmat.2022.129871.

[4] Q.Q. Zhang, G.G. Ying, C.G. Pan, Y.S. Liu, J.L. Zhao, Comprehensive evaluation of antibiotics emission and fate in the river basins of China: source analysis, multimedia modeling, and linkage to bacterial resistance, Environ. Sci. Technol. 49 (11) (2015) 6772–6782, https://doi.org/10.1021/acs.est.5b00729.

[5] E. Hain, H. Adejumo, B. Anger, J. Orenstein, L. Blaney, Advances in antimicrobial activity analysis of fluoroquinolone, macrolide, sulfonamide, and tetracycline antibiotics for environmental applications through improved bacteria selection, J. Hazard. Mater. 415 (2021), 125686, https://doi.org/10.1016/j.jhazmat.2021.125686.

[6] W. Qian, W. Hu, Z. Jiang, Y. Wu, Z. Li, Z. Diao, M. Li, Degradation of tetracycline hydrochloride by a novel $CDs/g-C_3N_4/BiPO_4$ under visible-light irradiation: reactivity and mechanism, Catalysts 12 (7) (2022) 774, https://doi.org/10.3390/catal12070774.

[7] J. Tang, J. Fang, N.F. Tam, Y. Yang, Y. Dai, J. Zhang, Y. Shi, Impact of phytoplankton blooms on concentrations of antibiotics in sediment and snails in a Subtropical River, China, Environ. Sci. Technol. 55 (3) (2021) 1811–1821, https://doi.org/10.1021/acs.est.0c08248.

[8] Y. Zhou, Y. Gao, J. Jiang, Y.-M. Shen, S.-Y. Pang, Z. Wang, J. Duan, Q. Guo, C. Guan, J. Ma, Transformation of tetracycline antibiotics during water treatment with unactivated peroxymonosulfate, Chem. Eng. J. 379 (2020) 122378, https://doi.org/10.1016/j.cej.2019.122378.

[9] Y. Zeng, E. Almatrafi, W. Xia, B. Song, W. Xiong, M. Cheng, Z. Wang, Y. Liang, G. Zeng, C. Zhou, Nitrogen-doped carbon-based single-atom Fe catalysts: synthesis, properties, and applications in advanced oxidation processes, Coord. Chem. Rev. 475 (2023), 214874, https://doi.org/10.1016/j.ccr.2022.214874.

[10] W. Xia, B. Song, H. Yi, E. Almatrafi, Y. Yang, Y. Fu, X. Huo, F. Qin, L. Xiang, Y. Zeng, G. Zeng, C. Zhou, From aquatic biota to autogenous N-doping biochar—using a highly efficient nonradical dominant process for sulfamethoxazole degradation, J. Clean. Prod. 373 (2022), 133750, https://doi.org/10.1016/j.jclepro.2022.133750.

[11] Y. Park, C. Kim, M. Kim, S. Kim, W. Choi, Ambient-temperature catalytic degradation of aromatic compounds on iron oxide nanorods supported on carbon nanofiber sheet, Appl. Catal., B 259 (2019), 118066, https://doi.org/10.1016/j.apcatb.2019.118066.

[12] C. Cheng, S. Gao, J. Zhu, G. Wang, L. Wang, X. Xia, Enhanced performance of $LaFeO_3$ perovskite for peroxymonosulfate activation through strontium doping towards 2,4-D degradation, Chem. Eng. J. 384 (2020), 123377, https://doi.org/10.1016/j.cej.2019.123377.

[13] M. Kohantorabi, G. Moussavi, S. Giannakis, A review of the innovations in metal- and carbon-based catalysts explored for heterogeneous peroxymonosulfate (PMS) activation, with focus on radical vs. non-radical degradation pathways of organic contaminants, Chem. Eng. J. 411 (2021) 127957, https://doi.org/10.1016/j.cej.2020.127957.

[14] H. Zhou, L. Lai, Y. Wan, Y. He, G. Yao, B. Lai, Molybdenum disulfide (MoS_2): a versatile activator of both peroxymonosulfate and persulfate for the degradation of carbamazepine, Chem. Eng. J. 384 (2020), 123264, https://doi.org/10.1016/j.cej.2019.123264.

[15] H. Xia, Z. Zhang, J. Liu, Y. Deng, D. Zhang, P. Du, S. Zhang, X. Lu, Novel Fe-Mn-O nanosheets/wood carbon hybrid with tunable surface properties as a superior catalyst for Fenton-like oxidation, Appl. Catal. B 259 (2019), 118058, https://doi.org/10.1016/j.apcatb.2019.118058.

[16] C. Guan, J. Jiang, C. Luo, S. Pang, Y. Yang, Z. Wang, J. Ma, J. Yu, X. Zhao, Oxidation of bromophenols by carbon nanotube activated peroxymonosulfate (PMS) and formation of brominated products: comparison to peroxydisulfate (PDS), Chem. Eng. J. 337 (2018) 40–50, https://doi.org/10.1016/j.cej.2017.12.083.

[17] M. Jiang, J. Li, Y. Zhao, L. Pan, Q. Cao, D. Wang, Y. Du, Double perovskites as model bifunctional catalysts toward rational design: the correlation between electrocatalytic activity and complex spin configuration, ACS Appl. Mater. Interfaces 10 (23) (2018) 19746–19754, https://doi.org/10.1021/acsami.8b05353.

[18] S.B. Hammouda, F. Zhao, Z. Safaei, V. Srivastava, D. Lakshmi Ramasamy, S. Iftekhar, S. Kalliola, M. Sillanpää, Degradation and mineralization of phenol in aqueous medium by heterogeneous monopersulfate activation on nanostructured cobalt based-perovskite catalysts $ACoO_3$ (A = La, Ba, Sr and Ce): characterization, kinetics and mechanism study, Appl. Catal. B 215 (2017) 60–73, https://doi.org/10.1016/j.apcatb.2017.05.051.

[19] X. Hu, M. Li, Y. Xie, Y. Yang, X. Wu, C. Xia, Oxygen-deficient Ruddlesden-Popper-type lanthanum strontium cuprate doped with bismuth as a cathode for solid oxide fuel cells, ACS Appl. Mater. Interfaces 11 (24) (2019) 21593–21602, https://doi.org/10.1021/acsami.9b05445.

[20] J. García, G. Subías, J. Blasco, M.C. Sánchez, G. Beutier, Resonant x-ray scattering study of charge superstructures in layered $La_{2-x}Ca_xCoO_{4\pm\delta}$ ($0.4 \leq x \leq 0.7$) and $La_{1.5}Sr_{0.5}CoO_4$ compounds, Phys. Rev. B 97 (8) (2018) 085111, https://doi.org/10.1103/PhysRevB.97.085111.

[21] M. Hammad, B. Alkan, A.K. Al-kamal, C. Kim, M.Y. Ali, S. Angel, H.T. A. Wiedemann, D. Klippert, T.C. Schmidt, C.W.M. Kay, H. Wiggers, Enhanced heterogeneous activation of peroxymonosulfate by Ruddlesden-Popper-type $La_2CoO_{4+\delta}$ nanoparticles for bisphenol A degradation, Chem. Eng. J. 429 (2022), 131447, https://doi.org/10.1016/j.cej.2021.131447.

[22] L. Yang, X. Jiao, X. Xu, Y. Pan, C. Su, X. Duan, H. Sun, S. Liu, S. Wang, Z. Shao, Superstructures with atomic-level arranged perovskite and oxide layers for advanced oxidation with an enhanced non-free radical pathway, ACS Sustain. Chem. Eng. 10 (5) (2022) 1899–1909, https://doi.org/10.1021/acssuschemeng.1c07605.

[23] H.X. Chen, Y. Xu, K.M. Zhu, H. Zhang, Understanding oxygen-deficient $La_2CuO_{4-\delta}$ perovskite activated peroxymonosulfate for bisphenol a degradation: the role of localized electron within oxygen vacancy, Appl. Catal., B 284 (2021) 119732, https://doi.org/10.1016/j.apcatb.2020.119732.

[24] K. Wang, C. Han, Z.P. Shao, J.S. Qiu, S.B. Wang, S.M. Liu, Perovskite oxide catalysts for advanced oxidation reactions, Adv. Funct. Mater. 31(30), 2102089, doi:https://doi.org/10.1002/adfm.202102089.

[25] Y. Zhao, B. Huang, H. An, G. Dong, J. Feng, T. Wei, Y. Ren, J. Ma, Enhanced activation of peroxymonosulfate by Sr-doped $LaFeO_3$ perovskite for Orange I degradation in the water, Sep. Purif. Technol. 256 (2021), 117838, https://doi.org/10.1016/j.seppur.2020.117838.

[26] P. Gao, S. Yan, X. Tian, Y. Nie, Y. Wang, Y. Deng, J. Tu, Identification and manipulation of active centers on perovskites to enhance catalysis of peroxymonosulfate for degradation of emerging pollutants in water, J. Hazard. Mater. 424 (Pt A) (2022), 127384, https://doi.org/10.1016/j.jhazmat.2021.127384.

[27] L. Zhang, L. Zhang, Y. Sun, B. Jiang, Porous ZrO_2 encapsulated perovskite composite oxide for organic pollutants removal: enhanced catalytic efficiency and suppressed metal leaching, J. Colloid Interface Sci. 596 (2021) 455–467, https://doi.org/10.1016/j.jcis.2021.03.171.

[28] Y. Zhao, D. Wu, Y. Chen, Y. Li, X. Fan, F. Zhang, G. Zhang, W. Peng, Thermal removal of partial nitrogen atoms in N-doped graphene for enhanced catalytic oxidation, J. Colloid Interface Sci. 585 (2021) 640–648, https://doi.org/10.1016/j.jcis.2020.10.043.

[29] Y. Liu, R. Qu, X. Li, X. Wei, L. Feng, A bifunctional $\beta-MnO_2$ mesh for expeditious and ambient degradation of dyes in activation of peroxymonosulfate (PMS) and

simultaneous oil removal from water, J. Colloid Interface Sci. 579 (2020) 412–424, https://doi.org/10.1016/j.jcis.2020.06.073.

[30] H. Shan, X. Dong, X. Cheng, Y. Si, J. Yu, B. Ding, Highly flexible, mesoporous structured, and metallic Cu-doped C/SiO2 nanofibrous membranes for efficient catalytic oxidative elimination of antibiotic pollutants, Nanoscale 11 (31) (2019) 14844–14856, https://doi.org/10.1039/c9nr04118d.

[31] X. Li, X. Yan, X. Hu, R. Feng, M. Zhou, L. Wang, Hollow Cu-Co/N-doped carbon spheres derived from ZIFs as an efficient catalyst for peroxymonosulfate activation, Chem. Eng. J. 397 (2020), 125533, https://doi.org/10.1016/j.cej.2020.125533.

[32] L. Zhang, N. Yang, Y. Han, X. Wang, L. Zhang, Y. Sun, B. Jiang, Highly dispersed β-FeOOH nanocatalysts anchored in confined membrane pores for simultaneously improving catalytic and separation performance, Sep. Purif. Technol. 279 (2021), 119684, https://doi.org/10.1016/j.seppur.2021.119684.

[33] S. Zheng, H. Chen, X. Tong, Z. Wang, J.C. Crittenden, M. Huang, Integration of a photo-Fenton reaction and a membrane filtration using CS/PAN@FeOOH/g-C3N4 electrospun nanofibers: synthesis, characterization, self-cleaning performance and mechanism, Appl. Catal. B 281 (2021), 119519, https://doi.org/10.1016/j.apcatb.2020.119519.

[34] S. Wang, J. Tian, Q. Wang, F. Xiao, S. Gao, W. Shi, F. Cui, Development of CuO coated ceramic hollow fiber membrane for peroxymonosulfate activation: a highly efficient singlet oxygen-dominated oxidation process for bisphenol a degradation, Appl. Catal., B 256 (2019) 117783, https://doi.org/10.1016/j.apcatb.2019.117783.

[35] Y. Han, B. Jiang, C. Zhang, L. Zhang, L. Zhang, Y. Sun, N. Yang, Co@N-C nanocatalysts anchored in confined membrane pores for instantaneous pollutants degradation and antifouling via peroxymonosulfate activation, J. Water Process Eng. 47 (2022), 102639, https://doi.org/10.1016/j.jwpe.2022.102639.

[36] Y. Huan, S. Chen, R. Zeng, T. Wei, D. Dong, X. Hu, Y. Huang, Intrinsic effects of Ruddlesden-Popper-based bifunctional catalysts for high-temperature oxygen reduction and evolution, Adv. Energy Mater. 9 (29) (2019) 1901573, https://doi.org/10.1002/aenm.201901573.

[37] L. Zhang, N. Yang, Y. Han, X. Wang, S. Liu, L. Zhang, Y. Sun, B. Jiang, Development of polyacrylonitrile/perovskite catalytic membrane with abundant channel-assisted reaction sites for organic pollutant removal, Chem. Eng. J. 437 (2022), 135163, https://doi.org/10.1016/j.cej.2022.135163.

[38] M. Sánchez-Andújar, M.A.A. Señarıs-Rodrıguez, Synthesis, structure and microstructure of the layered compounds Ln$_{1-x}$Sr$_{1+x}$CoO4 (Ln: La, Nd and Gd), Solid State Sci. 6 (1) (2004) 21–27, https://doi.org/10.1016/j.solidstatesciences.2003.11.005.

[39] V.N. Stathopoulos, V.C. Belessi, T.V. Bakas, S.G. Neophytides, C.N. Costa, P. J. Pomonis, A.M. Efstathiou, Comparative study of La–Sr–Fe–O perovskite-type oxides prepared by ceramic and surfactant methods over the CH4 and H2 lean-deNO$_x$, Appl. Catal., B 93 (1-2) (2009) 1–11, https://doi.org/10.1016/j.apcatb.2009.09.003.

[40] Z. Teng, Z. Xiao, G. Yang, L. Guo, X. Yang, R. Ran, W. Wang, W. Zhou, Z. Shao, Efficient water splitting through solid oxide electrolysis cells with a new hydrogen electrode derived from A-site cation-deficient La$_{0.4}$Sr$_{0.55}$Co$_{0.2}$Fe$_{0.6}$Nb$_{0.2}$O$_{3-\delta}$ perovskite, Mater. Today Energy 17 (2020) 100458, https://doi.org/10.1016/j.mtener.2020.100458.

[41] S. Ding, M. Li, W. Pang, B. Hua, N. Duan, Y.-Q. Zhang, S.-N. Zhang, Z. Jin, J.-L. Luo, A-site deficient perovskite with nano-socketed Ni-Fe alloy particles as highly active and durable catalyst for high-temperature CO2 electrolysis, Electrochim. Acta 335 (2020), 135683, https://doi.org/10.1016/j.electacta.2020.135683.

[42] J.S.B. Melbiah, D. Nithya, D. Mohan, Surface modification of polyacrylonitrile ultrafiltration membranes using amphiphilic Pluronic F127/CaCO3 nanoparticles for oil/water emulsion separation, Colloids Surf. A Physicochem. Eng. Asp. 516 (2017) 147–160, https://doi.org/10.1016/j.colsurfa.2016.12.008.

[43] A. Noormohamadi, M. Homayoonfal, M.R. Mehrnia, F. Davar, Synergistic effect of concurrent presence of zirconium oxide and iron oxide in the form of core-shell nanoparticles on the performance of Fe3O4@ZrO2 /PAN nanocomposite membrane, Ceram. Int. 43 (18) (2017) 17174–17185, https://doi.org/10.1016/j.ceramint.2017.09.142.

[44] H. Lin, Q. Fang, W. Wang, G. Li, J. Guan, Y. Shen, J. Ye, F. Liu, Prussian blue/PVDF catalytic membrane with exceptional and stable Fenton oxidation performance for organic pollutants removal, Appl. Catal., B 273 (2020), 119047, https://doi.org/10.1016/j.apcatb.2020.119047.

[45] W.-D. Oh, Z. Dong, T.-T. Lim, Generation of sulfate radical through heterogeneous catalysis for organic contaminants removal: current development, challenges and prospects, Appl. Catal., B 194 (2016) 169–201, https://doi.org/10.1016/j.apcatb.2016.04.003.

[46] P. Hu, M. Long, Cobalt-catalyzed sulfate radical-based advanced oxidation: a review on heterogeneous catalysts and applications, Appl. Catal. B 181 (2016) 103–117, https://doi.org/10.1016/j.apcatb.2015.07.024.

[47] L. Lai, J. Yan, J. Li, B. Lai, Co/Al2O3-EPM as peroxymonosulfate activator for sulfamethoxazole removal: performance, biotoxicity, degradation pathways and mechanism, Chem. Eng. J. 343 (2018) 676–688, https://doi.org/10.1016/j.cej.2018.01.035.

[48] R. Zhang, Y. Wan, J. Peng, G. Yao, Y. Zhang, B. Lai, Efficient degradation of atrazine by LaCoO3/Al2O3 catalyzed peroxymonosulfate: performance, degradation intermediates and mechanism, Chem. Eng. J. 372 (2019) 796–808, https://doi.org/10.1016/j.cej.2019.04.188.

[49] L. Zhang, Y. Zhang, J. Wei, W. Liu, Perovskite LaFe$_x$Co$_{1-x}$O$_{3-\lambda}$ deposited SiO2 catalytic membrane for deeply cleaning wastewater, Chem. Eng. J. 403 (2021), 126386, https://doi.org/10.1016/j.cej.2020.126386.

[50] T. Matsushita, W. Sugita, T. Ishikawa, G. Shi, S. Nishizawa, Y. Matsui, N. Shirasaki, Prediction of 1,4-dioxane decomposition during VUV treatment by model simulation taking into account effects of coexisting inorganic ions, Water Res. 164 (2019), 114918, https://doi.org/10.1016/j.watres.2019.114918.

[51] Q. Pan, Q. Gao, G. Gao, M. Liu, B. Han, K. Xia, C. Zhou, Composition-engineered LaCoO3-based monolithic catalysts for easily operational and robust peroxymonosulfate activation, Chem. Eng. J. 424 (2021), 130574, https://doi.org/10.1016/j.cej.2021.130574.

[52] N. Lu, H. Lin, G. Li, J. Wang, Q. Han, F. Liu, ZIF-67 derived nanofibrous catalytic membranes for ultrafast removal of antibiotics under flow-through filtration via non-radical dominated pathway, J. Membr. Sci. 639 (2021), 119782, https://doi.org/10.1016/j.memsci.2021.119782.

[53] W. Qin, G. Fang, Y. Wang, D. Zhou, Mechanistic understanding of polychlorinated biphenyls degradation by peroxymonosulfate activated with CuFe2O4 nanoparticles: key role of superoxide radicals, Chem. Eng. J. 348 (2018) 526–534, https://doi.org/10.1016/j.cej.2018.04.215.

[54] M. Zhu, J. Miao, X. Duan, D. Guan, Y. Zhong, S. Wang, W. Zhou, Z. Shao, Postsynthesis growth of CoOOH nanostructure on SrCo$_{0.6}$Ti$_{0.4}$O$_{3-\delta}$ perovskite surface for enhanced degradation of aqueous organic contaminants, ACS Sustain. Chem. Eng. 6 (11) (2018) 15737–15748, https://doi.org/10.1021/acssuschemeng.8b04289.

[55] X. Duan, C. Su, J. Miao, Y. Zhong, Z. Shao, S. Wang, H. Sun, Insights into perovskite-catalyzed peroxymonosulfate activation: maneuverable cobalt sites for promoted evolution of sulfate radicals, Appl. Catal. B 220 (2018) 626–634, https://doi.org/10.1016/j.apcatb.2017.08.088.

[56] G. Geng, M. Cai, R. Fang, Q. Luan, Z. Zhang, J. Song, J. Zhang, Metal-organic frameworks-derived perovskite catalysts for efficient degradation of 2, 4-dichlor-ophenol via peroxymonosulfate activation, Appl. Surf. Sci. 534 (2020), 147467, https://doi.org/10.1016/j.apsusc.2020.147467.